*Aust. J. Phys.*, 1995, **48**, 1027–43

# Oscillating Apparent Horizons in Numerically Generated Spacetimes*

*Peter Anninos, David Bernstein,*[C] *Steve Brandt,*[B] *David Hobill,*[A]
*Ed Seidel*[B] *and Larry Smarr*[B]

National Center for Supercomputing Applications, 605 E. Springfield Avenue,
Champaign, Illinois 61801, USA.
[A] Department of Physics and Astronomy, University of Calgary,
Calgary, Alberta T2N 1N4, Canada.
[B] Department of Physics, University of Illinois at Urbana-Champaign,
Urbana, Illinois 61801, USA.
[C] Department of Mathematics, Statistics and Computing Science,
University of New England, Armidale, NSW 2351, Australia.

*Abstract*

We investigate the evolution of the apparent horizon in three families of numerically generated spacetimes: the 'black hole plus Brill wave' spacetimes of Bernstein *et al.*, the non-time symmetric generalisation of this by Brandt, and the Misner two black hole spacetime. Various measures of the curvature and shape of the horizon are shown as a function of coordinate time at infinity and it is found that the horizon oscillates at the lowest quasinormal mode frequency of the hole. In addition, in the spacetimes with angular momentum the total angular momentum of the final hole can be read off from the oscillations of the horizon directly without having to extract it from the gravitational radiation emitted by the hole.

## 1. Introduction

The numerical relativity group at the National Center for Supercomputing Applications has been investigating the dynamics of vacuum black hole spacetimes with numerical techniques since the mid 1980s. These efforts have now produced several interesting results which have recently been published (Abrahams *et al.* 1992; Anninos *et al.* 1993*a*, 1993*b*, 1993*c*, 1994*a*, 1994*b*; Bernstein and Tod 1994; Bernstein *et al.* 1992, 1994*a*; Seidel and Suen 1994). This paper may be considered as a summary of several of those publications (in particular Anninos *et al.* 1994*a*). One of the main areas of research is in the evolution of vacuum spacetimes containing black holes. In this area the group has focused its efforts on two families of spacetimes: the study of spacetimes containing a single hole interacting with a gravitational wave (the black hole plus Brill wave spacetimes) and the two black hole spacetimes whose initial data were first constructed by Misner (1960). In addition the black hole plus Brill wave family has been broadened by Brandt (Brandt and Seidel 1995; Anninos *et al.* 1994*a*) to include angular momentum and so this family now contains the Kerr spacetime, the spacetimes generated by the Bowen and York (1980) initial data, as well as

* Refereed paper based on a contribution to the inaugural Australian General Relativity Workshop held at the Australian National University, Canberra, in September 1994.

0004-9506/95/061027$10.00

other spacetimes describing distorted rotating holes. In this paper we discuss the evolution of the apparent horizon in a few representative members of these spacetimes. All of the computations are carried out in the 3+1 formalism and some relevant information on this has been put into the Appendix. Descriptions of numerical algorithms, code tests, etc., are contained in our other work (Abrahams *et al.* 1992; Anninos *et al.* 1993*b*, 1995*b*; Bernstein 1993; Bernstein and Tod 1994; Bernstein *et al.* 1994*b*).

## 2. The Spacetimes

Each of the spacetimes we investigate contain either one or two black holes, the number being primarily dependent on the choice of topology of the $t =$ constant hypersurfaces of the spacetimes. In this section we briefly describe some of the geometrical and physical characteristics of each of the initial data sets which generate the spacetimes.

Initial data for the black hole plus Brill wave spacetime is obtained by putting the initial 3–metric $\gamma_{ab}$ (for notation see Appendix) in a form similar to that studied by Brill (1959):

$$ds^2 = \Psi^4[e^{2q}(d\eta^2 + d\theta^2) + \sin^2\theta d\phi^2] \tag{1}$$

[i.e., $A = B = e^{2q}$, $D = 1$, and $F = 0$ in equation (A2)]. The function $q(\eta, \theta)$ is arbitrary up to boundary conditions, a fall-off rate, and a possible restriction in magnitude (Bernstein 1993; Bernstein *et al.* 1994*a*). One obtains initial data by specifying $q$ and solving the Hamiltonian constraint for the conformal factor $\Psi$. We choose the function $q(\eta, \theta)$ to have the form

$$q(\eta, \theta) = Q_0 g(\eta) \sin^n\theta\,, \tag{2}$$

where we use the 'inversion symmetric Gaussian'

$$g(\eta) = \exp\left[-\left(\frac{\eta+\eta_0}{\sigma}\right)^2\right] + \exp\left[-\left(\frac{\eta-\eta_0}{\sigma}\right)^2\right] \tag{3}$$

for the radial function $g$. Symmetry considerations require $n$ to be a positive, even integer. We have investigated spacetimes with $n = 2$ and $n = 4$; however in this paper we consider those with $n = 2$ only. As discussed in the Appendix, the initial slice has the hypercylinder topology familiar from the maximally extended Schwarzschild solution. Thus there are two isometric, asymptotically flat 'sheets' connected by a 'throat', a 2–sphere which because of the isometry of the two sheets is minimal. For these initial data sets the throat is located at $\eta = 0$ and the isometry is $\eta \to -\eta$.

The function $g$ has three parameters which, roughly speaking, specify the amplitude $Q_0$, range $\eta_0$ and width $\sigma$ of the wave. (We note that in other papers related to this work the amplitude is denoted by $a$, but here we use $Q_0$ to avoid confusion with the usual angular momentum parameter $a$ that is used in describing rotating black holes in this paper.) One regains the Schwarzschild spacetime by setting $Q_0 = 0$, in which case the Hamiltonian constraint has the solution

$$\Psi = \sqrt{2m}\cosh(\eta/2)\,, \tag{4}$$

where $m$ is a length scale parameter which, in this case, is equal to the mass of the hole (and also the ADM mass of the spacetime). Some properties of the apparent horizon in these initial data sets are discussed in Section 3. For a more thorough discussion the reader is referred to our earlier work (Bernstein 1993; Bernstein and Tod 1994; Bernstein *et al.* 1994*a*).

These data sets have been generalised to include extrinsic curvature and angular momentum by Brandt (Brandt and Seidel 1995). We transform the the Kerr metric via

$$r = r_+ \cosh^2(\eta/2) - r_- \sinh^2(\eta/2)\,, \tag{5}$$

$$r_\pm = m \pm \sqrt{m^2 - a^2}\,, \tag{6}$$

where $a$ is the standard Kerr angular momentum parameter and $m$ is the mass of the Kerr black hole. With this transformation the spatial part of the Kerr metric can be written as

$$ds^2 = \Psi^4[e^{-2q_0}(d\eta^2 + d\theta^2) + \sin^2\theta d\phi^2]\,, \tag{7}$$

where

$$\Psi^4 = g^{(K)}_{\phi\phi}/\sin^2\theta\,, \tag{8}$$

$$\Psi^4 e^{-2q_0} = g^{(K)}_{rr}\left(\frac{dr}{d\eta}\right)^2 = g^{(K)}_{\theta\theta}\,, \tag{9}$$

and $g^{(K)}_{\mu\nu}$ is the Kerr metric in Boyer–Lindquist coordinates (see Misner *et al.* 1973). Notice that if the angular momentum parameter in the Boyer–Lindquist metric vanishes then $q_0 = 0$ and we recover the Schwarzschild 3-metric.

We can now generalise the metric (8) to include a Brill wave by adding a function $q(\eta, \theta)$ in a manner similar to equation (1)

$$ds^2 = \Psi^4[e^{2(q-q_0)}(d\eta^2 + d\theta^2) + \sin^2\theta d\phi^2]\,. \tag{10}$$

In this context, the parameter $q_0$ is interpreted as the Brill wave required to make the initial slice conformally flat. By setting $q = Q_0 g(\eta)\sin^n\theta + q_0$, where $g(\eta)$ is given by (3), we can add a Brill wave to these data sets in the same way one was added to the Schwarschild spacetime above.

For these data sets we have a non-zero extrinsic curvature and in general the Hamiltonian and momentum constraints will be coupled. A specific choice of the conformal form of the extrinsic curvature will decouple the constraints and under these conditions simple solutions to the momentum constraint which may be obtained include the Bowen and York (1980) solution and the Kerr solution.

Finally, we have the two black hole initial data sets of Misner (1960). These are a single parameter family of time symmetric data sets with 3–metric

$$ds^2 = \Psi_M^4(d\rho^2 + dz^2 + \rho^2 d\phi^2)\,, \tag{11}$$

where

$$\Psi_M = 1 + \sum_{n=1}^{\infty} \frac{1}{\sinh(n\mu)}\left(\frac{1}{{}^{+}r_n} + \frac{1}{{}^{-}r_n}\right), \tag{12}$$

and

$${}^{\pm}r_n = \sqrt{\rho^2 + [z \pm \coth(n\mu)]^2}\,. \tag{13}$$

The topology of the initial slice is that of two asymptotically flat sheets joined by two throats. As discussed below, if the two throats are far enough apart the spacetime generated is that of two nonrotating equal mass black holes colliding head-on along the $z$-axis.

The free parameter $\mu$ is related to the ADM mass of the spacetime

$$M = 4\sum_{n=1}^{\infty} \frac{1}{\sinh(n\mu)}\,, \tag{14}$$

and the proper distance along the spacelike geodesic connecting the throats

$$L = 2\left(1 + 2\mu \sum_{n=1}^{\infty} \frac{n}{\sinh(n\mu)}\right). \tag{15}$$

Increasing $\mu$ sets the two black holes further away from one another and decreases the total mass of the system.

Our calculations of colliding black holes are performed using the Čadež (1971) coordinates and the metric in this set of coordinates can be written in the form of equation (A2) as

$$ds^2 = \Psi^4(d\eta^2 + d\theta^2 + D\sin^2\theta\ d\phi^2)\,, \tag{16}$$

where $\Psi^4 = \Psi_M^4/J$, $D = J\rho^2/\sin^2\theta$ and $J = (\partial\eta/\partial\rho)^2 + (\partial\eta/\partial z)^2$ is the Jacobian of the two coordinate systems.

The advantage of Čadež coordinates is that they are boundary fitted coordinates designed to conform naturally to the spatial geometry of the two throats. They are spherical near the throats of the holes and further out in the wave zone, thus allowing us to handle throat boundaries and asymptotic wave form extractions in a convenient way. Their disadvantage is a singular point introduced by the coordinate transformation at the origin ($\rho = z = 0$). This presents certain numerical difficulties that will not be discussed here. Instead, we refer the interested reader to Anninos *et al.* (1993*b*, 1995*b*) for a thorough discussion of our numerical methods.

## 3. Apparent Horizons

A compact orientable 2–surface is said to be marginally trapped if its outward pointing null normal has zero divergence and on an asymptotically flat slice the apparent horizon is defined to be the outermost marginally trapped surface

(Hawking 1973; Cook and York 1990). It is well known that the apparent horizon must lie inside of an event horizon in any spacetime not containing a naked singularity (Hawking 1973). Unlike the event horizon, the apparent horizon may be located on a given slice of a 3+1 foliation without computing the entire spacetime, and in axisymmetry this makes the location of apparent horizons a comparatively simple exercise. A number of researchers have investigated the existence, location and physical properties of apparent horizons in a variety of initial data sets (Čadež 1974; Bernstein *et al.* 1994*a*; Bishop 1982; Cook 1990; Cook and York 1990).

Once the horizon has been found we may compute several standard measures of its intrinsic geometry in order to understand its shape and how it changes in time. In particular, we may compute the embedding diagram of the horizon, its Gaussian curvature $\kappa$ and its polar and equatorial circumferences $C_p$ and $C_e$. In axisymmetry the latter two are well defined since the $\phi$ = constant curves and the curve $\theta = \pi/2$ are geodesics of the surface. The quantities are

$$C_p = 4\int_0^{\pi/2} \Psi^2 \sqrt{A\left(\frac{dh}{d\theta}\right)^2 + B + \frac{F^2}{D}}\, d\theta\,, \tag{17}$$

$$C_e = 2\pi\Psi^2\sqrt{D}\,, \tag{18}$$

evaluated at $\theta = \pi/2$, and we define $C_r$ to be their ratio

$$C_r = C_p/C_e\,. \tag{19}$$

In (17), $h(\theta)$ is the coordinate position of the apparent horizon. Calculation of the Gaussian curvature $\kappa$ of the horizon is performed in a similarly straightforward manner.

Typically in our spacetimes the area of the apparent horizon grows with time due to a numerical effect which is well-understood but difficult to circumvent (see e.g. Bernstein 1993; this is not a numerical instability but rather a certain type of error which is difficult to control). This causes the Gaussian curvature of the horizon to decrease with time (for a sphere the Gaussian curvature is just $4\pi$ divided by the area) and we choose to normalise it in the following way. Let $A_{AH}$ and $M_{AH}$ be the proper area and mass of the apparent horizon as defined below (19). We compute the angular momentum parameter $a/M_{AH}$ from the known total angular momentum $J$. From this we compute the Gaussian curvature of the equilibrium solution with that mass and angular momentum parameter (i.e. from the Kerr solution). With no rotation this is just $4\pi/A_{AH}$ which is $(2M_{AH})^{-2}$. We then divide the Gaussian curvature of the horizon by this equilibrium quantity normalised to $4\pi$. In spherical symmetry, therefore, the 'area normalised Gaussian curvature' will take on the value $4\pi$, independent of the area of the horizon. Henceforth, when we refer to Gaussian curvature, we have normalised it in this way.

We also compute the embedding diagram of the horizon in a flat 3–space. We construct a 2–surface in the flat space with the same intrinsic geometry as the apparent horizon, thereby obtaining a 'picture' of the horizon. Once it has been determined that the embedding exists, construction of the diagram is obtained by standard methods (Eppley 1977; Smarr 1973). The embedding diagrams are also 'normalised' in a manner similar to the Gaussian curvature, by plotting the flat-space coordinates in units of a characteristic mass which we take to be the ADM mass $M$ (20) [or the apparent horizon mass $M_{AH}$ in equation (22) when numerical effects cause it to become larger than $M$].

The total mass and angular momentum of the spacetime are evaluated using the ADM integrals (O'Murchada and York 1974)

$$M = -\frac{1}{2\pi}\oint_S \nabla_a \Psi dS^a \,, \tag{20}$$

$$P_a = \frac{1}{8\pi}\oint_S \sqrt{\gamma}(K_{ab} - \gamma_{ab}\mathrm{tr}K)dS^b \tag{21}$$

($\gamma = \det\gamma_{ab}$) at the outer edge of our grid. As long as gravitational waves do not propagate beyond the outer boundary (20) will remain constant. In axisymmetry, with $\partial/\partial\phi$ the Killing vector, the component $P_\phi$ is the total angular momentum which we denote by $J$. Gravitational radiation cannot carry angular momentum in axisymmetry and so $J$ should be strictly constant.

As noted above, the apparent horizon will, in general, lie inside the event horizon so that calculating the area of the apparent horizon should provide a lower bound on the area of the event horizon (this is strictly true on a time symmetric slice). We follow Christodoulou (1970) and others by defining the mass of the apparent horizon by

$$M_{AH} = \sqrt{\frac{A_{AH}}{16\pi} + \frac{4\pi J^2}{A_{AH}}} \,, \tag{22}$$

where $J$ is the angular momentum of the spacetime and $A_{AH}$ is the area of the apparent horizon. The mass of the black hole, $M_{BH}$, is defined by replacing $A_{AH}$ by the area of the event horizon in (22). On a given slice the difference between the mass of the apparent horizon(s) and the ADM mass provides a measure of the size of the black hole(s) relative to that of the remaining gravitational wave energy on the slice. Since we expect the final state of the evolution of any of our initial data sets to be a static or stationary hole plus gravitational radiation propagating to future null infinity, we will have

$$M = M_{BH} + M_{rad} \,, \tag{23}$$

where $M_{rad}$ is the total time integrated energy loss through a 2–sphere far from the throat(s). If $M_{BH}$ is approximated by $M_{AH}$, then (23) can be used to obtain an upper bound on the amount of gravitational radiation which reaches future null infinity.

As far as our three initial data sets are concerned we have the following situation: In the black hole plus Brill wave data set the apparent horizon may either be prolate (data sets with $Q_0$ positive) or oblate ($Q_0$ negative). The ratio of circumferences can be quite extreme, exceeding 100 in the former case and approaching zero in the latter case. In general the horizon lies on the throat but if $|Q_0|$ is large enough it may detach from the throat and move outwards (in these cases the throat may either be a stable or unstable minimal surface). In the data sets with rotation the apparent horizon has similar properties depending on just what sub-family of data sets one is computing. In the case of the Kerr data set the apparent horizon is oblate and the ratio of circumferences may be computed analytically (Smarr 1973). In the two black hole data sets the horizon consists of either one or two 2–spheres depending on whether the parameter $\mu$ is less than or greater than about $1\cdot36$. In the former case it is always prolate with a maximum $C_r$ of about $2\cdot0$. More detail on the geometry of the apparent horizon is given in (Anninos *et al.* 1993*b*, 1993*c*; Seidel and Suen 1994).

## 4. Evolution of the Apparent Horizon

For the evolution we look at four cases: two black hole plus Brill wave spacetimes,

$$\text{Case (1)}: Q_0 = 0\cdot1, \quad \eta_0 = 0, \quad \sigma = 1\cdot0, \quad n = 2,$$

$$\text{Case (2)}: Q_0 = 1\cdot0, \quad \eta_0 = 0, \quad \sigma = 1\cdot0, \quad n = 2,$$

a case with angular momentum,

$$\text{Case (3)}: Q_0 = 1\cdot0, \quad n = 2, \quad \sigma = 1, \quad \eta_0 = 0, \quad J = 5\cdot5$$

and a two black hole spacetime,

$$\text{Case (4)}: \mu = 2\cdot2 \quad (L/M = 4\cdot46).$$

Cases (1) and (2) study the effect of a Brill wave of varying amplitude interacting with a hole. The wave is initially centred on the throat, which is the apparent horizon for these two data sets, and this causes an initial prolate distortion of the horizon. As discussed in Bernstein (1993) and Bernstein *et al.* (1994*a*) both of these cases contain predominantly the $\ell = 2$ angular modes, where $\ell$ is the index of the spherical harmonic $Y_{\ell m}$ (the corresponding data sets with $n = 4$ contain much stronger $\ell = 4$ and higher angular modes).

In Fig. 1 we show the evolution of the ratio of circumferences $C_r$ for case (1). The solid curve represents the numerical result, while the dashed curve shows a fit to the fundamental and first overtone of the $\ell = 2$ quasi-normal mode frequencies known from perturbation theory (Chandrasekhar 1983). The phase and amplitude of both modes is computed by a least squares fit. We see that the initially distorted hole relaxes to a spherical shape in a damped oscillatory fashion and the 'wavelength' and 'damping time' of the ratio of circumferences are very close to those of the fundamental $\ell = 2$ quasi-normal mode frequency ($16\cdot8M$ and $11\cdot2M$ respectively; in this case the ADM mass is very close to the final apparent horizon mass and we use '$M$' for both). Note that the time in Fig. 1 is the coordinate time of the $t =$ constant slices on which the apparent horizon is found. This corresponds to the proper time at the grid edge, where the lapse function is close to unity; in the region where the apparent horizon is located the maximal slicing lapse is in the neighborhood of $0\cdot3$. Note also that, strictly speaking, the apparent horizon is a *spacelike* hypersurface and so has no intrinsic timelike direction. Thus it cannot be said to be oscillating in the usual sense of the word although it does have a 'wavelength' (perhaps 'corrugated' is more apt).

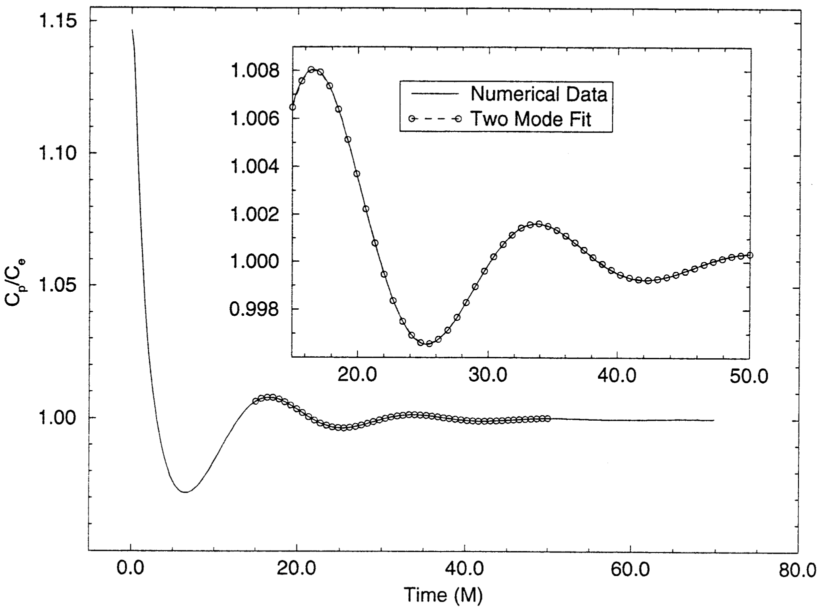


**Fig. 1.** We show the ratio of polar to equatorial circumferences $C_r$ of the apparent horizon as a function of time for case (1). The inset shows a least squares fit to the two lowest $\ell = 2$ quasi-normal mode frequencies.

The fact that in these spacetimes the apparent horizon oscillates with the quasi-normal frequency of the black hole (with respect to the coordinate time $t$) can be easily understood. As a perturbing source approaches the hole (in this case a gravitational wave), the background spacetime geometry is disturbed. The quasi-normal modes are excited, originating at the peak of the gravitational scattering potential $V(r)$, located outside the horizon at $r = 3M$ (Chandrasekhar 1983). Gravitational waves at the quasi-normal frequency are then sent in both directions away from the peak of $V(r)$, towards the horizon on one side and towards null infinity on the other side. Those waves going across the horizon induce a shearing of its surface, causing its geometry to oscillate at the same frequency as the waves. As the time slicing is essentially fixed in time from the horizon out to infinity during this oscillation phase, the 'background' spacetime can be considered essentially static and spherical. (Although coordinates are falling towards the hole and metric functions are growing in time, the horizon itself is a geometric structure that is static in the spherical limit. Its coordinate location may change as coordinates fall towards the hole, but its geometric position does not.) Under these conditions we expect the horizon to oscillate at the quasi-normal frequency in coordinate time as the ingoing waves cross it. Therefore, under many circumstances we expect to be able to use the apparent horizon as a probe to explore the dynamics of the black hole spacetime. The same dynamics have been seen in the geometry of the event horizon, as reported in Anninos *et al.* (1995*a*).

In Fig. 2 we show the 'area normalised Gaussian curvature' of the apparent horizon (as described in Section 3) as a function of the polar angle $\theta$ and coordinate time for case (1). Here the shading is such that the minimum curvature

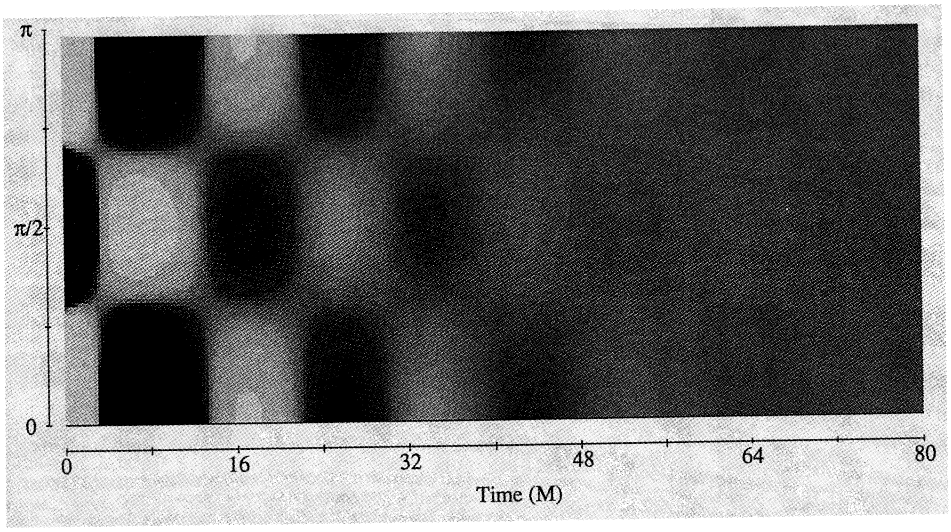


**Fig. 2.** Gaussian curvature of the apparent horizon is plotted as a function of the polar angle $\theta$ and coordinate time for case (1). As discussed in the text, the 'box' pattern is typical for the predominantly $\ell = 2$ distortion. The period of the oscillation of $16{\cdot}8M$ can be seen in the diagram.

is mapped to white, the maximum is mapped to black and intermediate values are represented by shades of grey (the equilibrium value $4\pi$ is represented by a medium shade of grey). This map is used to bring out the dynamics as the horizon settles down to its equilibrium shape (which is a sphere for the spacetimes discussed in this section). The $n = 2$ spacetime in Fig. 2 has a distinct 'box' pattern indicating that the normalised curvature oscillates between greater than and less than $4\pi$, around what appears to be a fixed line of latitude on the horizon which has a value close to $\pi/3$. Consequently there are moments of time where the apparent horizon is momentarily spherical (has constant Gaussian curvature). Note that the apparent horizons of spacetimes generated with other values of $n$ in (2) generate qualitatively different plots of this kind. For data sets with $n = 4$ in (2) the 'box' pattern is replaced by an 'X' pattern which is the result of a higher amount of $\ell = 4$ mode in the initial data.

We have verified that these patterns are to be expected for these spacetimes by expanding the metric in terms of a spherical background piece $\overset{o}{g}_{\alpha\beta}$ and a non-spherical perturbation piece which is written as an expansion in terms of the usual Regge–Wheeler perturbation functions (Chandrasekhar 1983). We note that in our perturbed spacetimes the apparent horizon lies on approximately constant radial coordinate surfaces and we can easily compute the Gaussian curvature on such surfaces from the perturbation expansion. If we assume the perturbation is a superposition of the various $\ell$ modes, each oscillating at the appropriate quasi-normal frequency, we obtain the following expressions for the Gaussian curvature to lowest perturbative order:

$$\kappa_{\ell=2} = \frac{1}{R^2}\left(2 + \frac{K}{2}\sqrt{\frac{5}{\pi}}(1 + 3\cos 2\theta)e^{-i\omega t}\right), \tag{24}$$

$$\kappa_{\ell=4} = \frac{1}{R^2}\left(2 + \frac{27K}{64\sqrt{\pi}}(9 + 20\cos 2\theta + 35\cos 4\theta)e^{-i\omega t}\right). \tag{25}$$

These expressions generate the characteristic 'box' pattern for a pure $\ell = 2$ perturbation and the 'X' pattern for an admixture of $\ell = 2$ and $\ell = 4$ perturbations, as expected. From the $\ell = 2$ pattern, there is a line of constant curvature at $\theta = 0{\cdot}5\cos^{-1}(-\frac{1}{3}) \sim \pi/3$, which is observed as noted above. Thus, these diagrams are very useful in identifying the various oscillation modes present in the horizon, as different modes have qualitatively different patterns.

Case (2) is the high amplitude version of case (1). Fig. 3 shows the corresponding $C_r$ and the least squares $\ell = 2$ mode fit. The hole is much more distorted initially than case (1), but almost all of the initial distortion is shed by $t = 5M$ off the initial slice and by about $t = 20M$ or so the hole is oscillating in the $\ell = 2$ mode like case (1).

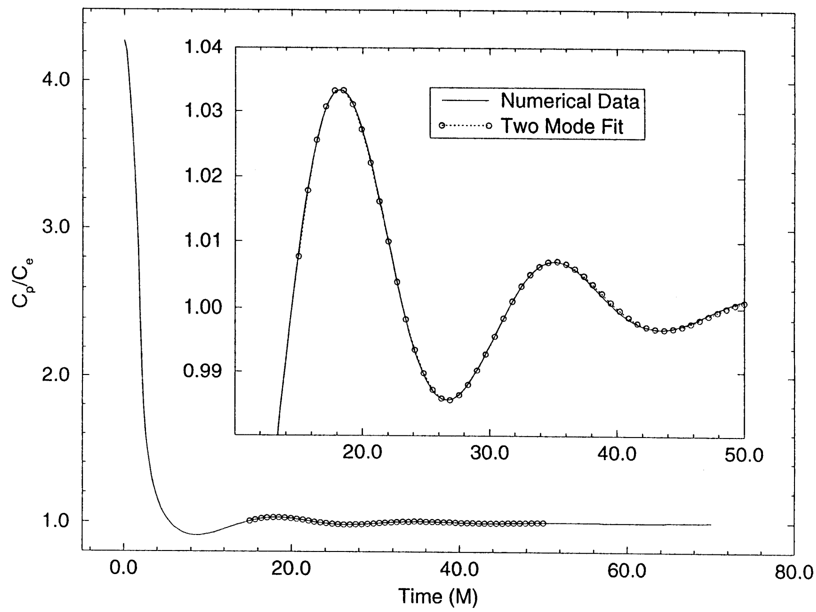


**Fig. 3.** Ratio of circumferences $C_r$ of the apparent horizon is shown as a function of time for case (2). The amplitude of the wave is larger in this case, causing a much larger distortion of the hole.

We can also construct a geometric embedding of the apparent horizon in a three dimensional Euclidean space, as mentioned in Section 3. Fig. 4 shows the horizon embedding for a sequence of time slices. On the initial slice the horizon is quite prolate. The surface quickly evolves towards a more spherical configuration, and then begins to oscillate at the quasi-normal frequency about its spherical equilibrium shape, going from slightly oblate to slightly prolate and back, eventually settling down to a sphere. At $t = 40M$ the hole is quite spherical, as the figure indicates.

Case (3) is a rotating version of case (2) with $J/M^2 = 0{\cdot}39$. We note that $J/M^2$ is equivalent to $a/m$ in the standard Boyer Lindquist notation (see e.g. Misner *et al.* 1973). In Fig. 5 we show $C_r$ for this case. As we explain in the following paragraphs, the hole is not oscillating about $C_r = 1$, as in the non-rotating case, but about some other equilibrium value related to its rotation.

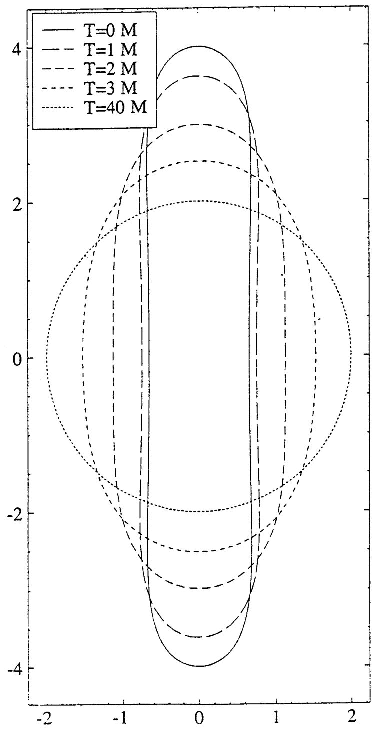


**Fig. 4.** We show cross sections of the geometric embedding of the horizon in a flat 3D space, at various times, for case (2). Initially the hole is quite prolate, but it quickly evolves towards a more spherical shape, when it begins to oscillate at the quasi-normal frequency of the hole.

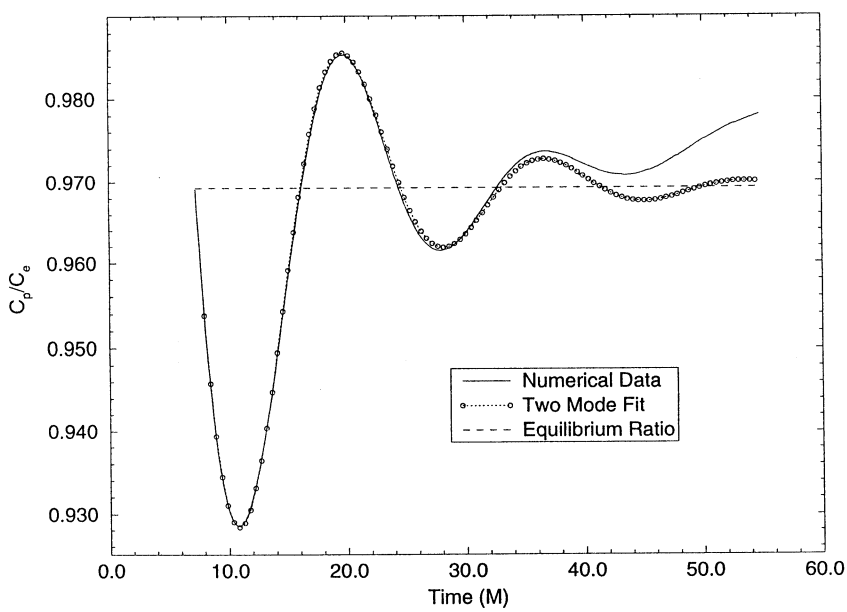


**Fig. 5.** We show the ratio of circumferences $C_r$ of the apparent horizon as a function of time for case (3). This is a rotating version of case (2). The long dashed line shows the offset required by the quasi-normal mode fit.

[Note that the slight upward drifting of $C_r$ at late times is due to numerical difficulties in computing the area of the horizon as described in Section 3 and in more detail in Brandt and Seidel (1995).] The long dashed line denotes the value of the constant offset or equilibrium ratio required by the $\ell = 2$ fit to $C_r$.

In fitting $C_r$ to the lowest two quasi-normal modes we included corrections for the wavelength due to rotation (Seidel and Iyer 1990). The quasi-normal frequencies of rotating black holes depend on their angular momentum as well as their mass, but the dependence on the angular momentum is extremely weak except for large rotation rates in which $a/m \sim 1$. As a result, corrections due to rotation rates for the cases that we have studied here are slight and they make no significant impact to the fitted wave modes. Thus it is difficult to determine the angular momentum of the hole from the wavelength of the quasi-normal mode except in cases of extreme rotation. However, using the formula in Smarr (1973), one can use the shape of the horizon itself much more effectively in this regard. The larger the rotation parameter, the more oblate the horizon becomes. This effect provides a means to extract the value of $J/M^2$ from the apparent horizon. The procedure for doing this begins by computing $C_r$ and its offset from unity and then using the results of Smarr (1973) to estimate the rotation parameter, which we denote by $(J/M^2)_{(C_r)}$. We can also estimate the mass of the hole $M$ from $C_e$, which allows us to solve for the angular momentum $J$ strictly in terms of measurements of the horizon geometry. Because $C_e$ settles down to $4\pi M$ as the horizon approaches equilibrium we can represent $C_e/4\pi$ as $M_{(C_e)}$. Then $J$ is computed by the formula

$$J = (J/M^2)_{(C_r)} M^2_{(C_e)}\,, \tag{26}$$

which works well throughout the evolution.

We find that the value of $J$ extracted from the horizon surface by using this procedure agrees with the input parameter specified in solving the momentum constraint to within a few per cent for all cases studied. Therefore, simply by making measurements of the geometric shape of the horizon we can accurately estimate the mass and angular momentum of the black hole. Alternatively, in cases like this where we know the angular momentum of the hole, specified in an initial value procedure, we can measure the shape of the horizon, compute the offset value of the oscillations, and compare with the analytic results of Smarr (1973). However, in a more general three-dimensional case, where angular momentum can be radiated by gravitational waves, the angular momentum of the hole cannot be known as an input parameter, but could still be estimated in this way.

The final case is the spacetime generated by the Misner data with $\mu = 2{\cdot}2$. In this data set the apparent horizon consists of two disjoint 2–spheres and we have verified that this case represents two distinct black holes by integrating photons out along the equator ($z = 0$) from the origin ($z = \rho = 0$), making certain they propagate freely to $\rho \to \infty$ and are not trapped within the event horizon that forms to surround both holes during the merger process. The actual event horizon of this spacetime has been traced out and discussed in Anninos *et al.* (1995*a*). [The results for the two black hole spacetimes presented here are discussed in much more detail in (Anninos *et al.* 1993*c*, 1995*b*). There one can also find more general discussions of the total energies radiated, observed gravitational waveforms, horizon masses, etc., for a variety of initial configurations.]

In Fig. 6 we plot $C_r$ as a function of time for case (4). The horizon begins as two disjoint 2–spheres which merge at around $t = 8M$. After the merger the horizon quickly relaxes to a nearly spherical shape and begins quasi-normal mode oscillation in much the same way as case (2).

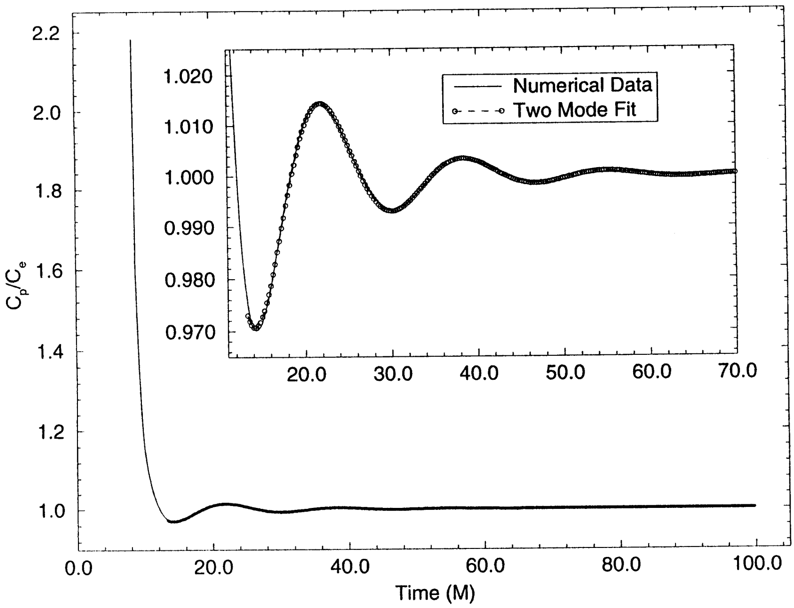


**Fig. 6.** Ratio of circumferences $C_r$ of the apparent horizon is shown as a function of time for case (4). The inset shows a least squares fit to the two lowest $\ell = 2$ quasi-normal mode frequencies.

One can draw comparisons between the colliding black hole spacetimes and the single black hole spacetimes discussed above. For example, case (4) is intermediate between cases (1) and (2) in terms of the initial merged horizon distortions. A more relevant comparison can be made with a Brill wave perturbation of amplitude $Q_0 \sim 0{\cdot}56$ ($\eta_0 = 0$, $\sigma = 1$, $n = 2$) which displays similar behaviour in the initial horizon distortions, the damping time to relax to the subsequent quasi-normal mode ringing, and in the amplitude of the mode ringing.

Fig. 7 shows the embedding diagrams for case (4) at various times as the horizon evolves from an initially disjoint configuration to a nearly static spherical state. At the initial time slice, the disjoint apparent horizons in Fig. 7 are the two throat positions. Because we use a lapse that is zero on both throats (as in the rotating black hole calculations), each throat remains a marginally trapped surface throughout the evolution with a 'frozen' intrinsic geometry. Our code does not distinguish among the different marginally trapped surfaces that may form outside the throats except where such surfaces intersect the equator ($z = 0$). As a result, the embedding diagrams remain constant in time until $t \sim 8M$ when the disjoint surfaces merge to form a single common horizon. The embeddings after the merger are normalised by the computed mass of the apparent horizon

$M_{AH}$ as described in Section 3. However, to maintain a sense of the relative scale of the initial two black holes to the final coalesced single hole, we choose to normalise the coordinates of the embedding diagrams before the merger ($t < 8M$) by the total ADM mass $M$.

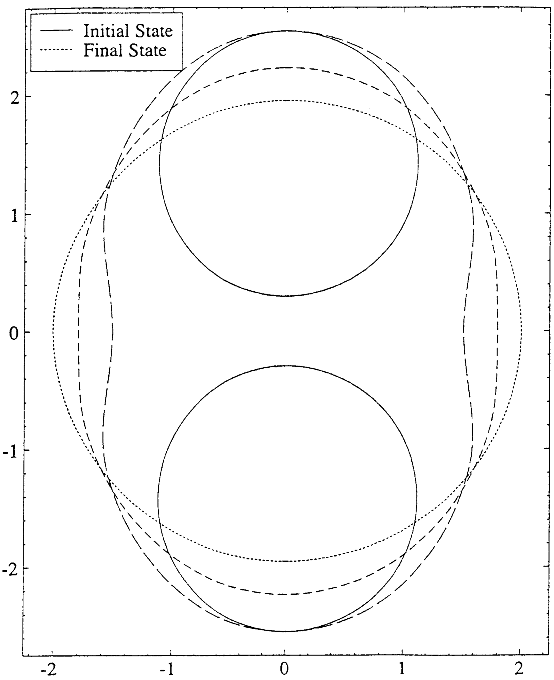


**Fig. 7.** We show the cross section of the horizon embedding for the two black hole collision case (4). At late times the final single black hole reaches a nearly static, spherical state.

## 5. Conclusions

From the results presented in Section 4, we can draw striking similarities between the $n = 2$ Brill wave perturbations of single rotating and nonrotating black holes and the collision of two equal mass black holes. The features common to the variety of spacetimes we have evolved include: (i) the initially highly distorted prolate/oblate horizon geometries quickly damp away towards an equilibrium shape (which is spherical for nonrotating holes and oblate for rotating holes), (ii) the horizon oscillates at a frequency that is predominantly the $\ell = 2$ quasi-normal mode frequency of the final state (or mass) of the black hole, and (iii) these oscillations damp away in time as the region near the event horizon emits gravitational radiation. The frequency and damping time of these oscillations can be found by examining the geometry of the apparent horizon. In fact, the consistency in our results over a range of various spacetimes with different time slicings (although all cases are maximal, the rotating and colliding black hole spacetimes use a lapse that is anti-symmetric across the throat while the non-rotating single black hole spacetimes use a lapse that is symmetric across the throat) suggests that all dynamic horizon geometries should have some generic features in common, particularly at late times when the dynamics are dominated by the quasi-normal ringing of the holes.

The fact that the horizons oscillate at the quasi-normal mode frequency can be understood from the standard picture of black hole perturbation theory. A disturbance in the gravitational field of a black hole generates gravitational waves at the peak of the gravitational scattering potential $V(r)$, which is located near $r = 3M$. These waves, emitted at the quasi-normal frequency of the hole, propagate away from the peak, down the hole on one side and away from the hole on the other side of the potential peak. The ingoing waves cause both a shearing and expansion of the black hole horizon, causing it to oscillate at the quasi-normal frequency.

We have shown that the apparent horizon can act as a powerful tool in understanding the dynamics of numerically generated black hole spacetimes. Measurements of its intrinsic geometry reveal not only the quasi-normal mode frequency of the hole, but also its mass and rotation parameter. The latter effect is particularly important, as the quasi-normal mode frequency is so weakly dependent on the rotation parameter that it is extremely difficult to extract from the oscillations themselves. On the other hand, the geometric shape of the horizon is sensitive to the rotation parameter, and can be used to extract information about the angular momentum of the hole. Furthermore, the oscillations in the Gaussian curvature of the horizon can be used to see at a glance the various $\ell$ modes present in the oscillation, as different modes have qualitatively different visual features.

The similarities between the colliding black hole spacetimes and the distorted single hole spacetimes indicate that the latter spacetimes are able to mimic the intermediate and late time behaviour of the collision of two black holes. The distorted single black hole spacetimes will continue to be explored as a guide to the physics of black hole collisions, without the complications introduced for studying the head-on two black hole collision.

Finally, we note that some animations and color images of horizon embedding diagrams for spacetimes like the ones presented in this paper are available on the NCSA relativity group World Wide Web server. The URL for our server is http://jean-luc.ncsa.uiuc.edu.

## Acknowledgments

We are pleased to acknowledge our colleagues who have contributed a number of helpful discussions throughout this work, including Andrew Abrahams, Joan Massó, and Wai-Mo Suen. These calculations were performed on the Cray Y-MP at NCSA and the C-90 at the Pittsburgh Supercomputing Center. This work has been supported by NCSA.

## References

Abrahams, A., Bernstein, D., Hobill, D., Seidel, E., and Smarr, L. (1992). *Phys. Rev.* D **45**, 3544.

Anninos, P., Bajuk, M., Bernstein, D., Hobill, D., Seidel, E., and Smarr, L. (1993*a*). *IEEE Comp. Graph. Appl.* **13**, 12.

Anninos, P., Hobill, D., Seidel, E., Smarr, L., and Suen, W.-M. (1993*b*). Technical Report No. 24, National Center for Supercomputing Applications (unpublished).

Anninos, P., Hobill, D., Seidel, E., Smarr, L., and Suen, W.-M. (1993*c*). *Phys. Rev. Lett.* **71**, 2851.
Anninos, P., Bernstein, D., Brandt, S., Hobill, D., Seidel, E., and Smarr, L. (1994*a*). *Phys. Rev.* D **50**, 3801.
Anninos, P., Bernstein, D., Hobill, D., Seidel, E., Smarr, L., and Towns, J. (1994*b*). *In* 'Numerical Astrophysics' (Eds W. Benz, J. Barnes, E. Muller, and M. Norman) (Springer: New York).
Anninos, P., Bernstein, D., Brandt, S., Libson, J., Massó, J., Seidel, E., Smarr, L., Suen, W.-M., and Walker, P. (1995*a*). *Phys. Rev. Lett.* **74**, 630.
Anninos, P., Hobill, D., Seidel, E., Smarr, L., and Suen, W.-M. (1995*b*). *Phys. Rev.* D **52**, 2044.
Bernstein, D. (1993). Ph.D. thesis, University of Illinois at Urbana-Champaign.
Bernstein, D., Hobill, D., Seidel, E., and Smarr, L. (1992). Sixth Marcel Grossman Meeting on General Relativity (Eds H. Sato and T. Nakamura), p. 1276 (World Scientific: Singapore).
Bernstein, D., Hobill, D., Seidel, E., and Smarr, L. (1994*a*). *Phys. Rev.* D **50**, 3760.
Bernstein, D., Hobill, D., Seidel, E., Smarr, L., and Towns, J. (1994*b*). *Phys. Rev.* D **50**, 5000.
Bernstein, D., and Tod, K. P. (1994). *Phys. Rev.* D **49**, 2808.
Bishop, N. T. (1982). *Gen. Rel. Grav.* **14**, 717.
Bowen, J., and York, J. W. (1980). *Phys. Rev.* D **21**, 2047.
Brandt, S., and Seidel, E. (1995). *Phys. Rev.* D **52**, 856.
Brill, D. S. (1959). *Ann. Phys.* **7**, 466.
Čadež, A. (1971). Ph.D. thesis, University of North Carolina at Chapel Hill.
Čadež, A. (1974). *Ann. Phys.* **83**, 449.
Chandrasekhar, S. (1983). 'The Mathematical Theory of Black Holes' (Oxford University Press: Oxford).
Christodoulou, D. (1970). *Phys. Rev. Lett.* **25**, 1596.
Cook, G. (1990). Ph.D. thesis, University of North Carolina at Chapel Hill.
Cook, G., and York, J. W. (1990) *Phys. Rev.* D **41**, 1077.
Eppley, K. (1977). *Phys. Rev.* D **16**, 1609.
Hawking, S. W. (1973). *In* 'Black Holes' (Eds C. DeWitt and B. S. Dewitt) (Gordon and Breach: New York).
Misner, C. (1960). *Phys. Rev.* **118**, 1110.
Misner, C. W., Thorne, K. S., and Wheeler, J. A. (1973). 'Gravitation' (W. H. Freeman: San Francisco).
O'Murchada, N., and York, J. (1974). *Phys. Rev.* D **10**, 2345.
Seidel, E., and Iyer, S. (1990). *Phys. Rev.* D **41**, 374.
Seidel, E., and Suen, W.-M. (1994). *Int. J. Mod. Phys.* C **5**, 181.
Smarr, L. L. (1973). *Phys. Rev.* D **7**, 289.

## Appendix

We use the 3+1 formalism whereby spacetime is viewed as a foliation by 3–surfaces each endowed with a positive definite 3–metric, $\gamma_{ab}$, and an extrinsic curvature tensor, $K_{ab}$. (Greek indices range from 0 to 3, Latin indices from 1 to 3. We work in geometrised units in which Newton's constant $G$ and the speed of light are equal to unity.) The spacetime metric takes the form

$$ds^2 = -(\alpha^2 - \beta^a\beta_a)dt^2 + 2\beta_a dx^a dt + \gamma_{ab}dx^a dx^b\,, \tag{A1}$$

where $\alpha$ (the 'lapse function') determines the foliation of the spacetime and $\beta^a$ (the 'shift vector') specifies three-dimensional coordinate transformations from slice to slice. In numerical relativity calculations it is common to choose the initial data and shift vector to eliminate certain components of $\gamma_{ab}$ and here we have chosen $\gamma_{12}$ and $\gamma_{13}$ to vanish. The $\gamma_{23}$ term is present only in the rotating case, carrying information about the odd-parity radiation modes present in that system. The resulting hypersurface line element is

$$
\begin{aligned}
dl^2 &= \gamma_{ab} dx^a dx^b \\
&= \Psi^4 (A d\eta^2 + B d\theta^2 + D \sin^2\theta d\phi^2 + 2F \sin\theta d\theta d\phi)\,.
\end{aligned}
\tag{A2}
$$

Here $(\eta, \theta, \phi)$ are spherical polar-like coordinates, $\eta$ is the logarithmic radial coordinate and $(\theta, \phi)$ the standard spherical polar coordinates on the $\eta =$ constant 2-spheres. The spacetime is assumed to possess an axial Killing vector $(\partial/\partial\phi)$. All the variables we work with are independent of $\phi$. In addition we choose not to evolve the conformal factor $\Psi$, hence this is a function of $\eta$ and $\theta$ only.

We specify the topology of the $t =$ constant hypersurfaces in the following way: the single non-rotating distorted hole and the single rotating distorted hole are given the 'single Einstein–Rosen bridge' ($\mathbf{S}^2 \times \mathbf{R}$) topology familiar from the Schwarzschild and Kerr spacetimes. The two black hole data sets of Misner possess the 'double Einstein–Rosen bridge' topology obtained by identifying the bottom sheets of two single bridges. In all three cases we compute each 3-metric such that there is an isometry between the top and bottom sheets. The 2-surface invariant under the isometry operation is called the throat and consists of one 2-sphere in the single bridge case and two disjoint 2-spheres in the double bridge case. In all cases we choose the throat to lie on a constant $\eta$ surface. This provides good boundary conditions for the 3-metric and extrinsic curvature components, $\alpha$, $\beta^a$, etc.

The conformal 3-metric components and their corresponding conformal extrinsic curvature components are evolved according to the 3+1 decomposition of the Einstein equations. The lapse function $\alpha$ is determined by using the maximal slicing condition, $\mathrm{tr}K = 0$. In the two cases where rotation is not present, the shift $\beta^a$ is chosen to make the remaining off-diagonal component of the 3-metric vanish. For the more general rotating case the shift is chosen to eliminate $\gamma_{12}$ and $\gamma_{13}$. It is not possible to eliminate both $\gamma_{13}$ and $\gamma_{23}$ in general radiating spacetimes (because they contain information about the odd-parity modes) and we choose to maintain a nonvanishing $\gamma_{23}$.

Finally, we choose each spacetime to be equatorially plane symmetric as well as axisymmetric and isometric through the throat(s). The computational domain is thus bounded by the axis ($\theta = 0$), the equator ($\theta = \pi/2$), the isometry surface, and an outer boundary, usually around $\eta = 6$ (but due to the logarithmic nature of $\eta$ this is large enough in terms of proper distance that static outer boundary conditions are adequate for the calculations carried out here). The numerical code to evolve the time symmetric (non-rotating) single bridge data sets has been described extensively elsewhere (Anninos *et al.* 1994*b*; Bernstein 1993; Bernstein *et al.* 1994*b*) and so we will not discuss our numerical methods here. Modifications to those methods for evolving the single bridge with rotation and the Misner two black hole initial data sets are detailed in Brandt and Seidel (1995) and Anninos *et al.* (1993*b*, 1995*b*) respectively.

Manuscript received 31 January, accepted 21 June 1995